Materials Science in Semiconductor Processing 137 (2022) 106189

Contents lists available at ScienceDirect

Materials Science in Semiconductor Processing

journal homepage: www.elsevier.com/locate/mssp

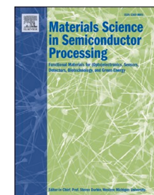

Indium tin oxide obtained by high pressure sputtering for emerging selective contacts in photovoltaic cells

D. Caudevilla [a], E. García-Hemme [a], E. San Andrés [a,*], F. Pérez-Zenteno [a], I. Torres [b], R. Barrio [b], R. García-Hernansanz [a], S. Algaidy [a], J. Olea [a], D. Pastor [a], A. del Prado [a]

[a] *Dpto. Estructura de la Materia, Física Térmica y Electrónica, Universidad Complutense de Madrid, Fac. de CC. Físicas. Plaza de Ciencias 1, E-28040 Madrid, Spain*
[b] *Unidad de Energía Solar Fotovoltaica, Dpto. de Energías Renovables, CIEMAT. Av/ Complutense 40, E-28040 Madrid, Spain*

ARTICLE INFO

Keywords:
High Pressure Sputtering
photovoltaics
transparent conductors
Selective contacts

ABSTRACT

This article studies the physical and electrical behavior of indium tin oxide layers (ITO) grown by an unconventional technique: High Pressure Sputtering (HPS), from a ceramic ITO target in a pure Ar atmosphere. This technique has the potential to reduce plasma induced damage to the samples. The aim is to obtain, at low temperature via HPS, good quality transparent conductive oxide layers for experimental photovoltaic cells with emerging selective contacts such as transition metal oxides, alkaline metal fluorides, etc. We found that the resistivity of the films was strongly dependent on Ar pressure. To obtain device-quality resistivity without intentional heating during deposition a pressure higher than 1.0 mbar was needed. These films deposited on glass were amorphous, presented a high electron mobility (up to 45 $cm^2V^{-1}s^{-1}$) and a high carrier density (2.9×10^{20} cm^{-3} for the sample with the highest mobility). The optimum Ar pressure range was found at 1.5–2.3 mbar. However, the resistivity degraded with a moderate annealing temperature in air. Finally, the feasibility of the integration with photovoltaic cells was assessed by depositing on Si substrates passivated by a-Si:H. The film deposited at 1.5 mbar was uniform and amorphous, and the carrier lifetime obtained was 1.22 ms with an implied open circuit voltage of 719 mV after a 215 °C air anneal. The antireflective properties of HPS ITO were also demonstrated. These results show that ITO deposited by HPS is adequate for the research of solar cells with emerging selective contacts.

1. Introduction

Heterojunction with intrinsic thin layer (HIT) photovoltaic cells are a particular structure that is being researched for increasing energy efficiency while maintaining a low levelized cost of energy (LCOE) [1,2]. In fact, there are commercial modules that are fabricated with this type of cells [3]. A particularity of these cells is the low temperature budget needed: the maximum processing temperature can be as low as 200 °C [3]. This presents several advantages, such as reduced silicon need because the wafers suffer less warping when annealing and, thus, can be cut thinner [4]. To further improve this kind of cells, a topic that is being researched is the substitution of the doped hydrogenated amorphous silicon (a-Si:H), used in the electron and hole contacts, by materials with a wider bandgap. In the standard HIT cell these doped regions are needed to produce carrier separation. However, the moderate bandgap of doped a-Si:H (around 1.7–1.9 eV [5,6]) produces parasitic blue light absorption at the illuminated side of the cell. These photogenerated carriers recombine before being separated, which leads to a reduction of the attainable short-circuit current. Thus, the research community is trying to achieve the carrier separation using materials with wider bandgaps. The structures that enable carrier separation are generally denominated selective contacts (SC). To separate the carriers there are emerging alternatives to the traditional *p-n* junction. For instance, materials that present large valence band offsets with minimal conduction band offsets, such as TiO_2 on n-Si [7]. Also, materials with extreme workfunction values that, in contact with Si, bend the bands upwards, such as MoO_x [8–11], WO_x [12] or V_2O_y [13], or downwards, such as LiF_x [7]. As first explained by Wurfel et al. [14,15], the first type of materials enhance the conductivity of holes while hindering the conductivity of electrons, and are used to substitute the p-doped a-Si:H. These materials are included in hole-selective contacts. Conversely, the materials used to enhance electron selectivity are used in electron-selective contacts. One of the first cells that used these structures was the Dopant-free Asymmetric Silicon Heterojunction solar cell

* Corresponding author.
E-mail address: esas@ucm.es (E. San Andrés).

https://doi.org/10.1016/j.mssp.2021.106189
Received 11 January 2021; Received in revised form 24 June 2021; Accepted 7 September 2021
Available online 15 September 2021
1369-8001/© 2021 The Authors. Published by Elsevier Ltd. This is an open access article under the CC BY-NC-ND license (http://creativecommons.org/licenses/by-nc-nd/4.0/).

(DASH). These cells initially showed conversion efficiencies under 14% [16–18]. However, Bullock et al. [19] significantly improved the efficiency to 19.4% by introducing MoO_x and LiF_x as hole and electron contacts, respectively. Since then, the efficiency of this structure has been improved to 20.7% [20]. In fact, cells with a 23.1% efficiency and an electron SC in the backside have been fabricated [7]. The factors affecting the efficiency of selective contacts have been studied theoretically [21,22], by simulation [23–25] and empirically [13,25,26].

Most of the emerging materials that produce carrier selectivity are semiconductors that have a moderate to high resistivity. Thus, to achieve low series resistance of the final cell, they have to be included with a limited thickness of only a few nm and have to be capped by a high conductivity layer to facilitate the lateral transport of the photogenerated carriers. For the top contact, this conductive layer needs also good transparency in the visible region, and usually it also acts as antireflective coating. The materials that achieve these characteristics are denominated Transparent Conductive Oxides (TCO) and are typically degenerated semiconductors [27]. If the cell is intended to be used in a bifacial configuration it needs to be transparent also at the bottom, so both sides of the cell must be covered by the TCO. The most widely used TCO is tin-doped indium oxide (ITO) [12,20,28]. At present, due to the scarcity of indium [29] and environmental and health concerns [30] there is a growing interest in indium-free TCOs, such as aluminum-doped zinc oxide (AZO) [31–33] and gallium doped zinc oxide (GZO) [34–36].

A critical step for the reliability of the fabrication process of the cell is the transfer from the selective contact deposition chamber to the TCO deposition equipment. During this transit, the film could be contaminated either by atmospheric exposure (for instance, by water absorption) or due to sample manipulation (C contamination). These spurious effects can lead to non-reproducible results. Thus, they could hinder the DASH cell development by introducing undesired non controlled parameters and obscuring the physical understanding of the processes. The goal of our research is to deposit both the material that provides selectivity and the TCO in the same novel HPS system without sample manipulation or exposing it to the atmosphere. As a first step, in this work we focus on the TCO material.

So far, the best results for hole-selective materials have been obtained with e-beam evaporated MoO_x [20], while the most widely used TCO material is ITO deposited by magnetron sputtering [10,12,20]. If these two different deposition techniques are used, the only way to avoid atmosphere exposure is by using expensive cluster systems that are unaffordable for most research laboratories and would impose a substantial increase in LCOE in an industrial plant. Low pressure conventional sputtering is a technique that presents some intrinsic advantages over evaporation: the targets can be fabricated with extremely high purity and no crucibles are needed, and, since the gas used is typically composed of high purity Ar, N_2 and O_2, film contamination can be minimal. The overall heating of the system is lower, so there is less desorption from walls to the processing atmosphere. The vacuum requirements are less stringent, due to the much higher working pressure. Non-elementary materials can be obtained with composite targets [37], by co-sputtering [38] or reactive sputtering [39], while in evaporation compositional control for most compounds is very difficult due to the very different vapor pressures of the elements. The cost in processing materials is lower, since the life of the sputtering target is larger than an equivalent e-beam crucible. Also, at the end of the target's life, the remaining material can be easily recycled (for expensive materials this is a great financial advantage). Finally, reverse sputtering can be used to clean *in-situ* the substrate before deposition. Due to these advantages, conventional magnetron sputtering is the technique most widely used to obtain high quality ITO, producing a low resistivity TCO with controlled damage to the substrate [40–43]. Also, some recent works are starting to study the deposition of MoO_x by sputtering [10,44]. If this would be achieved with reasonable material properties, then the sequential sputtering of SC/TCO would be a very interesting option for novel solar cell fabrication.

However, low pressure conventional sputtering has certain limitations, mainly the risk of permanent damage of the substrate surface by fast particles bombardment [43]. At typical sputtering pressures (10^{-2} – 10^{-3} mbar), the mean free path of the plasma species is in the order of some cm [45]. To avoid permanent plasma damage by non-thermalized species the sputtering power can be reduced or the sample can be separated from the plasma, but this leads to bigger processing chambers and/or a re-design of the sputtering source [40,43]. In this work we explore a non-conventional technique, HPS, that intends to minimize this issue by increasing substantially the working pressure, to the 0.5–5 mbar range. At these pressures, the mean free path is in the 10^{-2} cm range. Thus, the energetic sputtered species suffer many collisions within a short distance, decaying to their thermal energy and, from that point, they are transported to the substrate by a diffusion process. This way surface bombardment by un-thermalized particles is reduced, even at a very low distance from the target, and this enables the use of a compact processing chamber with less stringent vacuum requirements. This non-conventional technique was initially developed by Poppe et al. [46] for the epitaxial growth of YBaCuO, a high-T_c superconductor. Previously, we have successfully used it for the growth of high-*k* dielectrics such as TiO_2 [47], HfO_2 [48], Gd_2O_3 [49] or $Gd_xSc_{2\text{-}x}O_3$ [50]. In the DASH cell field, HPS can prevent permanent damage to the underlying a-Si:H passivation layer (if it is used in a TCO/SC/a-Si:H/c-Si configuration [51,52]), or to prevent interfacial defect creation (if the SC is directly deposited on c-Si [53–55]). In this work we have used HPS to deposit ITO at pressures in the mbar range, as a first step before depositing complete SC/TCO structures by sequential HPS deposition. To our knowledge, this is the first reported application of HPS in the SC field.

2. Experimental methods

ITO films were fabricated by means of HPS from a 2" ITO target (Kurt J. Lesker, 99.95% purity) sputtered in a pure Ar atmosphere. The target was bonded to the copper target holder with an Ag epoxy conductive resin (Testbourne). Due to the indirect target refrigeration the maximum *rf* power possible was 50 W. The sputtering pressure was varied in the range from 0.5 mbar to 2.3 mbar. The pressure was fixed by introducing the maximum Ar flow that our turbomolecular pump could withstand (80 sccm) and limiting the pumping speed with a guillotine valve. No intentional heating was applied to the sample. However, during the deposition process the refrigerated sample holder increased its temperature due to plasma heating. For instance, for the 50 W processes the temperature typically reached ~70 °C. The chamber was evacuated before sputtering to a base pressure lower than of 2×10^{-6} mbar. The *rf* power source used was a Hüttinger PFG 300 model working at 13.65 MHz, attached to a matchbox to minimize reflected power (the reflected power was less than 4 W for all processes). For each process we fixed the effective power that reaches the target, i. e. the difference between applied power and the reflected power.

The substrates used were square glasses of 2 cm side and 0.5 mm thick, or polished FZ n-Si 100 substrates with 1–3 Ω cm resistivity passivated on both sides with 5 nm of intrinsic a-Si:H deposited by plasma-enhanced chemical vapor deposition. Only for transmittance - reflectance measurements the films were deposited on square quartz of 2 cm side and 0.5 mm thick. The material was GE-124. All samples were cleaned with iso-propil alcohol and deionized water before introduction to the chamber. For residual water desorption, after introduction into the chamber, the bare glass samples were first heated in vacuum at 400 °C for 20 min. Just before the introduction to the HPS chamber the passivated Si samples were etched in a 1:50 HF solution during 30 s to remove the native oxide.

For the analysis of the species present in the plasma we used Glow Discharge Optical Emission (GDOS). Two independent spectrometers were used, model Blue-Wave from StellarNet, with wavelength ranges of

200–400 nm and 400–600 nm. The step was 0.25 nm. Each spectrometer was attached to a dedicated optical fiber with 1 mm diameter and 2 m long. The fibers were focused to the plasma through a sapphire window to ensure UV transmittance. The fiber attached to the 200–400 nm spectrometer was specific for the UV-VIS range.

For the electrical characterization, sheet resistance was measured by the 4-point probe method with an automated CMT-SR2000PV system. The probe separation was 1 mm, much larger than the film thickness and much smaller than the sample dimensions, thus the ideal correction factor π/ln 2 was used. The thickness of the films was obtained by measuring with a mechanical profilometer (Dektak) a step defined on the film by *in-situ* masking.

Also, the samples were cut in squares of 1 cm side and wire bonded with Ag paint in the four corners. We measured in darkness using a Keithley 4200 SCS equipped with four source and measure units connected to each contact. To obtain the sheet resistance we used the van der Pauw configuration: we introduced current ranging from 10 μA to 1 mA, depending on sample sheet resistance, between two contiguous contacts and measured the voltage difference in the opposite contacts. We measured the four different configurations applying the current in both directions. Following González-Díaz et al. [56] we corrected the total of eight configurations with the F factor. With the same setup we performed Hall effect measurements by introducing the current through two opposite contacts and measuring the voltage difference between the other two. The Hall effect was measured using a 0.9 T electromagnet powered by a Kepco 50 20 MG power source. To avoid thermo-galvanomagnetic effects, we measured the 8 configurations with the magnetic field in both directions, a total of 16 measurements. To study the thermal stability of the films, we performed several consecutive hot-plate annealings in air, with a duration of 30 min, at temperatures between 100 °C and 215 °C. After each anneal, the van der Pauw and Hall effect measurements were repeated. A first set of samples were deposited on glass, so substrate conductivity is negligible. Also, another set of ITO films were deposited on a-Si:H/c-Si/a-Si:H passivated substrates. Here, special care was taken to avoid that the Ag contacts could touch the c-Si substrate at the sample sides. This way, the ITO film was electrically separated from the c-Si wafer by the semi-insulating undoped a-Si:H film.

X-ray Photoelectron spectra (XPS) were recorded using a Fisons MT500 spectrometer equipped with a hemispherical electron analyzer (CLAM2) and a non-monochromatic Mg Kα X-Ray source operated at 300 W. The samples were fixed on small flat discs supported on an XYZ manipulator placed in the analysis chamber. The residual pressure in this ion-pumped analysis chamber was kept below 10^{-9} mbar during data acquisition. The spectra were collected at a pass energy of 20 eV, which is typical of high-resolution conditions. Spectra were analyzed using CasaXPS software. The intensities were estimated by calculating the area under each peak after subtraction of the S-shaped background and fitting the experimental curve to a combination of Lorentzian and Gaussian lines of variable proportions. Although specimen charging was observed, it was possible to determine accurate binding energies by referencing to the adventitious C1s peak at 285.0 eV. The maximum allowed variation of the binding energy was ±0.2 eV relative to the value specified for peak center. The atomic ratios were computed from the peak intensity ratios and the reported atomic sensitivity factors [57].

Grazing Incidence X-ray Diffraction (GI-XRD) patterns were measured with a PANalytical diffractometer X'Pert PRO MRD, using the Cu K_α line of 0.1541 nm. The incident angle was 0.1° and the 2θ angle was varied between 5° and 70°.

For the optical characterization of the ITO films, transmittance $T(\lambda)$ and specular reflectance $R(\lambda)$ spectra in the wavelength range from 300 to 2500 nm were obtained using a UV/Visible/NIR PerkinElmer Lambda 1050 spectrophotometer. Following J. L. Hernández et al. [58], the T - R results can be used to calculate the thickness of the film (and thus, growth rate) and the n values can be fitted to a Cauchy dispersion law. Once $n(\lambda)$ is known the absorption coefficient α can be calculated. From the $(\alpha^*E)^2$ vs E values [59,60] the optical bandgap can be obtained by fitting to a Tauc law [61].

To analyze the antireflective properties of the HPS ITO the hemispherical reflectance was also measured by the above-mentioned UV/Visible/NIR spectrophotometer with illumination from the ITO side. These measurements enabled the thickness calculation according to the following equation [62,63]:

$$nd = \lambda_{\min}/4 \tag{1}$$

Where n is the refraction index of the ITO films and $\lambda_{\min}$ the wavelength for which the hemispherical reflectance is minimum, between 300 and 1250 nm.

Minority carrier lifetime (τ) and implicit open-circuit at 1 sun (1-Sun iV_{oc}) of an ITO/a-Si:H/cSi/a-Si:H passivated sample were measured by means of the Quasi-Steady-State Photoconductance technique using a commercial setup (Sinton WCT-120) [64]. The measurements were taken before and after ITO deposition to assess the damage created during the deposition process and the control of surface recombination.

Finally, a cross sectional scanning electron microscopy (SEM) image of the annealed ITO/a-Si:H/c-Si/a-Si:H sample was obtained with a Jeol JSM 7600F operating at 15 kV. The sample was prepared by mechanically scribing the backside of the wafer and applying pressure afterwards until breakage.

3. Results and discussion

To examine the excited species presence and the stability of the plasma, a detailed plasma characterization was perfomed by GDOS. Also, we intended for each pressure to determine the onset of extraction of the species (the minimum *rf* power that is needed to start the target sputtering), and also it was used to check if both In and Sn were being effectively extracted at the several plasma conditions used.

Firstly, we found that the plasma started even at a low *rf* power of just 5 W. However, the minimum power needed to ionize Ar in the pressure range analyzed, and thus, achieve target sputtering, was between 25 and 30 W. This corresponds to ~1.25 W/cm^2. On the other hand, as explained in the experimental section, the maximum *rf* power is limited to 50 W. Thus, we studied the plasma in the 30 W–50 W range (1.5–2.5 W/cm^2).

Fig. 1 shows representative spectra of a typical sputtering process (conditions were pure Ar atmosphere, 1.0 mbar chamber pressure and *rf* power of 40 W) measured with the two spectrometers available. These spectra contain all the features that were found in the remaining conditions (although, as expected, the intensities were different depending on pressure and *rf* power). We observe that there were many emissions due to atomic transitions (narrow and intense peaks), but also some molecular emissions were present (wider peaks and with particular shapes for each molecule). We have labeled in the figure the main emissions of each detected species and in Table I we summarize the wavelengths of all the emissions identified in the plasma. Almost every single peak in the spectra has been identified, even some Ar and Ar^+ peaks that the reference tables mark as present with minimal intensity [65]. Due to coincidence of emissions, some peaks (304 nm, 305.25 nm) can be due either to In or Sn (or most likely, to a superposition of both).

The atomic species detected were Ar (neutral and ionized), In, Sn and O [65]. The molecular emissions of OH^- and NH were also found [66]. The wavelengths summarized in Table I were in excellent agreement with the tabulated references. Concerning the plasma stability, while the intensity of the atomic peaks remained stable during the processes, the intensity of the molecular emissions typically decreased with deposition time. This fact indicates that the latter were due to chamber contamination during sample load: during the process, due to heating and ultraviolet radiation, the walls degassed and the presence of molecules in the plasma decreased with the time. Thus, we will focus on atomic emissions.

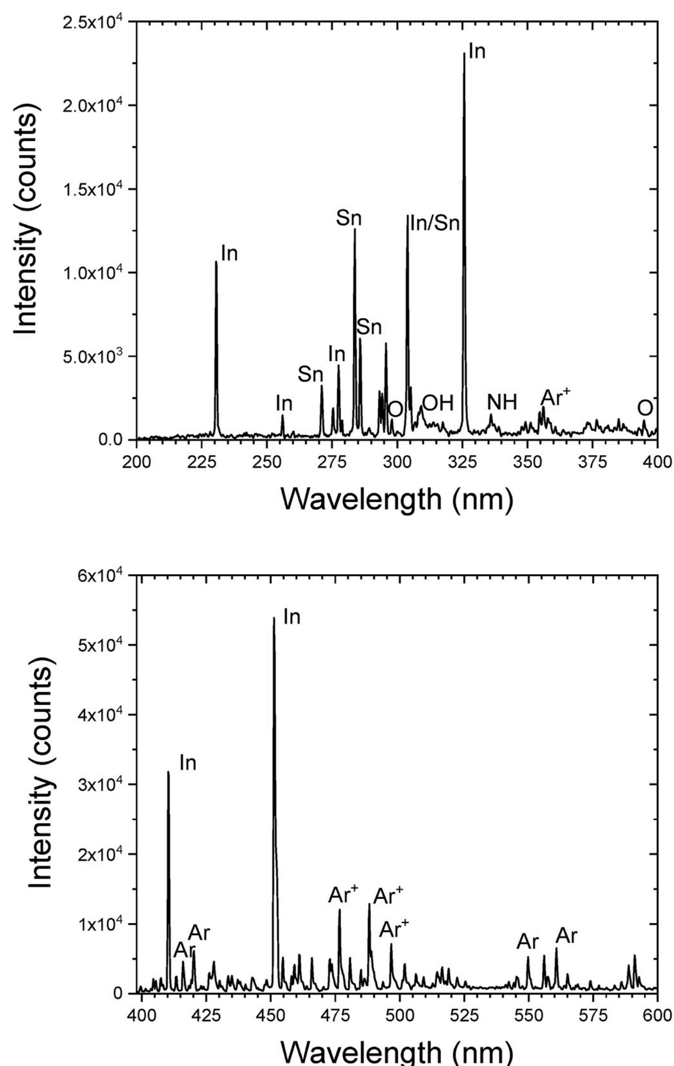

Fig. 1. Plasma emission as measured from GDOS of a process conducted at an Ar pressure of 1.0 mbar and a *rf* power of 40W in the range [200 nm–400 nm] (top) and [400 nm - 600 nm] (bottom). The most prominent emissions of the identified species are labeled.

Table 1
Identification of the main emissions detected in the plasmas [65].

Species	Emission (nm)
In	230.5, 256, 275.5, 277.5, 293.25, 295.75, 304, 305.25, 410.25, 451.25
Sn	271, 283.75, 285.75, 304, 305.25
Ar	416, 420.25, 519, 556, 549.75, 560.75, 565, 588.75, 591
Ar^+	294.5, 349.25, 351.25, 354.75, 356, 357.75, 413.25, 426.25, 428, 433.5, 435, 442.75, 454.75, 459.25, 461, 466, 473, 473.75, 476.75, 480.75, 485, 488, 496.75, 502, 506.25, 509, 514.5, 516.5, 522.25
O	298, 394.75
OH^-	band between 309 and 315
NH	band with peaks at 336, 337, 339

The emission did not change significantly in the pressure range studied (0.5 mbar–2.3 mbar). The same atomic emissions were found for all pressures. However, at 2.3 mbar the plasma was less stable, showing some random flickering in some processes. This effect could impact the repeatability of the results. This was an indication that this pressure was close to the limits of the system for the ITO target, thus the pressure was not increased further. The main conclusion that can be drawn from GDOS measurements is that sputtering ITO by HPS is feasible, since the ionized Ar produced the sputtering of In, Sn and O as evidenced by their presence in the plasma.

For typical solar cell applications ITO thickness is 80 nm with a sheet resistance of 100 Ω/□, which yields a resistivity of 8×10^{-4} Ω cm. Resistivity is determined by carrier concentration and mobility. The literature shows that in polycrystalline ITO the Sn content has a big impact on its resistivity: crystalline In_2O_3 is an electrical insulator, and the Sn atoms that get incorporated into the film introduce an excess of electrons that converts ITO in a degenerate n-type semiconductor. There are works showing that the resistivity strongly depends on the Sn content and its activation [67–69], with an optimal Sn/In atomic ratio around 0.1. This is the reason why the typical ITO target composition is 90% In_2O_3/10%SnO_2 in weight, which translates to an Sn/In atomic ratio of 0.102. On the other hand, in amorphous ITO the role of Sn is not so straightforward. Some works [69–71] found that in this amorphous material the oxygen vacancies determine the free carrier concentration, and that Sn is mainly inactive. Concerning the mobility, typically amorphous metals present lower values than their crystalline counterparts [8] because in the electronic cloud the electron mean free path is similar to the atomic distance [72]. However, this is not the case in amorphous ITO, where the main free path is in the order of 10 nm [73], so the scattering due to collisions with the lattice is negligible. Thus, amorphous ITO can present resistivity values comparable to polycrystalline ITO [73].

For our HPS deposited ITO, Fig. 2 shows the as-deposited resistivity as a function of pressure and *rf* power. The data were calculated from the sheet resistance value and the thickness. The thickness of the samples was in the 100–200 nm range. As expected, the growth rate was higher for the lower pressures.

Here we observe that the Ar pressure was the parameter that had the strongest impact on resistivity. For instance, at a fixed power of 40 W the resistivity variation was of more than two orders of magnitude. On the other hand, for a fixed pressure the differences with *rf* power were less than one order of magnitude for all pressures (for instance, at 1.5 mbar the resistivity range was 3–6×10^{-4} Ω cm). There is a noticeable change on resistivity when the deposition pressure changed from 0.75 mbar to 1.0 mbar. The minimum resistivity was obtained for pressures higher than 1.5 mbar with a value of 3×10^{-4} Ω cm. However, the film deposited at 2.3 mbar did not decrease resistivity significantly further.

The reason of the measured differences in resistivity with Ar pressure is not straightforward. Many works show that the ITO resistivity is low after annealing or deposition with elevated temperature [59,67,74,75]. These conditions result in polycrystalline films. In our films the substrate temperature was mainly determined by the *rf* power and it was quite

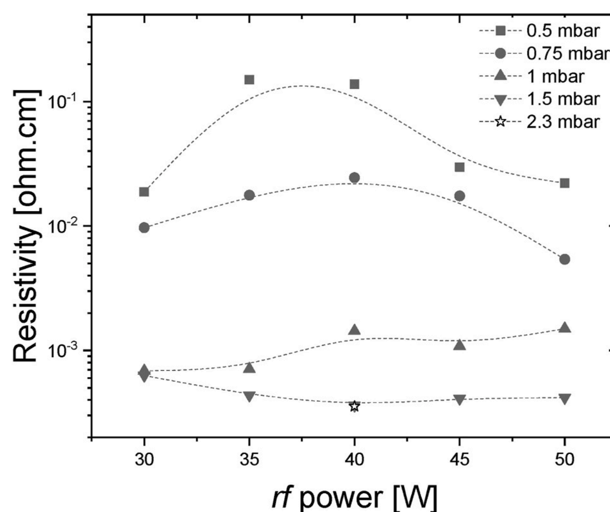

Fig. 2. Resistivity of the HPS deposited ITO films calculated from 4 point-probe measurements and profilometry as a function of *rf* power for several Ar pressures. Lines are guides to the eye.

low, always less than 75 °C. Also, for a fixed *rf* power the temperature difference between the different pressures was less than ~10 °C, so it cannot justify the large differences on resistivity measured. On the other hand, the growth rate varied almost an order of magnitude (from 3 nm/min at 0.5 mbar to 0.82 nm/min at 1.5 mbar for an *rf* power of 40 W). A fast growth rate can produce porosity that would increase resistivity [76]. Also, since the target to sample distance was not varied for all pressures, at lower pressures there is a higher chance that energetic species reach the growing film. This fast particle bombardment can affect the film growth by impacting on the nucleation, the polycrystallinity, the Sn incorporation at doping sites or the oxygen vacancy content. In the following we will attempt to rule out possible origins of the large resistivity change between 0.75 mbar and 1.5 mbar.

To explore if the change in resistivity can be attributed to a compositional change, we studied by XPS the Sn to In ratio in the range where resistivity variation was more pronounced, between 0.75 mbar and 1.5 mbar, and at a fixed *rf* power of 40W. No surface sputtering during the XPS measurement was available, so the information comes from the film top surface. Fig. 3 shows the XPS preliminary survey spectra of these samples, where the main transitions of each atom detected are indicated.

The first conclusion drawn was that no relevant differences were found for the measured films. For all films we found the C 1s peak at 284.8 eV, which shows the presence of adventitious carbon during the measurement. Besides, although all spectra present the O 1s peak, this signal was not reliable for the calculation of oxygen content of the film, due to water and NO_2 adsorption on the surface. The likely origin of this adventitious contamination is sample manipulation during cutting and transportation. Thus, we focused on the Sn to In ratio.

In Fig. 4 we show the 3d XPS peaks of In and Sn of the film deposited at 1.0 mbar. The fits of the $3d_{5/2}$ peaks are also shown. These fits were used to calculate the atomic Sn/In ratio. The results for the other pressures were very similar (not shown).

The results for the Sn/In ratio were 0.068 (0.75 mbar), 0.082 (1.0 mbar) and 0.070 (1.5 mbar). As a reference, in the target the atomic Sn/In ratio was 0.102. Considering the uncertainty of the fits, we can conclude from these results that in this pressure range there were no relevant differences in the Sn/In ratio. Thus, the observed differences in resistivity must arise from other sources.

To explore if we can relate the resistivity variation to changes in the crystallinity of the films, GIXRD measurements were performed, and the results are shown in Fig. 5. To ensure the maximum consistency between

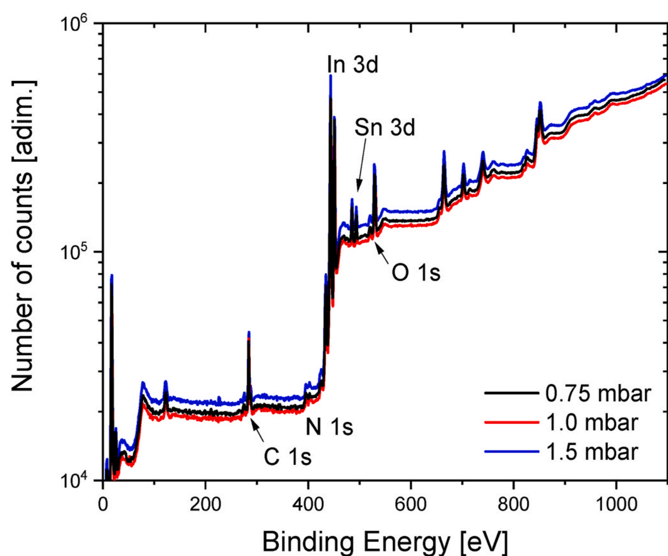

Fig. 3. XPS survey scan spectra for the ITO films deposited at pressures between 0.75 mbar and 1.5 mbar.

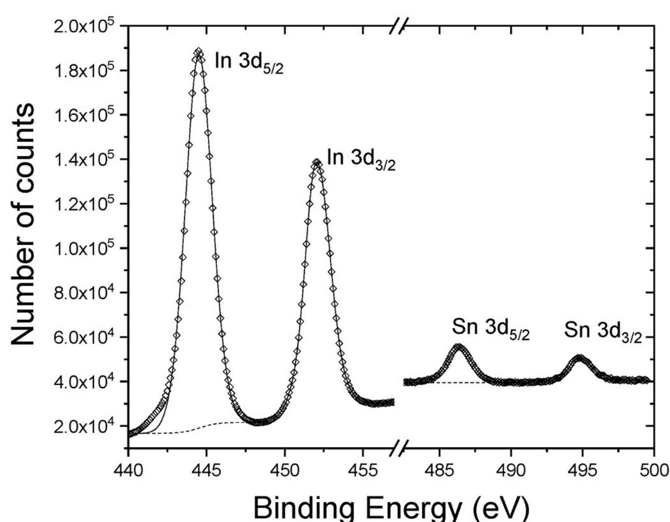

Fig. 4. XPS surface scan of the In 3d and Sn 3d regions or an ITO film sputtered at 1.0 mbar (open symbols). The dashed lines are the baselines and the solid lines are the peak fits used by CasaXPS for compositional calculation.

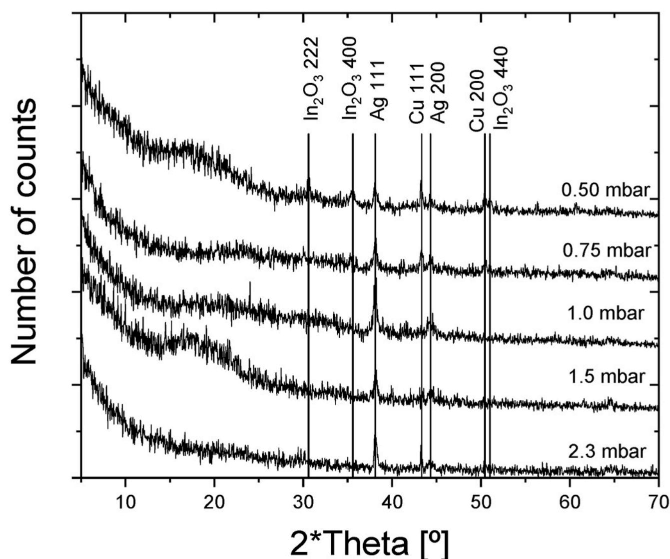

Fig. 5. GIXRD patterns of the same samples used for van der Pauw measurements. Only diffractions related to Ag (from Ag paste) or Cu (from cables) are detected, with the only exception of the 0.5 mbar sample, that shows the most intense cubic In_2O_3 peaks.

electrical and structural results, the samples characterized by GIXRD were the same square samples that were used for van der Pauw and Hall effect measurements. Thus, the samples had copper wires glued to the corners by silver paint.

As a consequence of using the samples prepared for electrical measurements, in every diffractogram we found the main peaks of cubic Cu [77] from the cables and cubic Ag [78] from the Ag paste used to connect the cables to the corners of the sample, that will not be further discussed. Some samples show a bump in the 15°-20° region, likely due to the glass substrate. These were the only diffractions found, with the only clear exception of the sample deposited at 0.5 mbar. This film showed clearly the (220), (400) and (440) In_2O_3 peaks [74,75], but with a low intensity. Also, the 0.75 mbar sample presents a peak at the (400) In_2O_3 diffraction, but with an intensity very close to the noise level. Thus, we can conclude that the ITO samples grown by HPS at a pressure of 1.0 mbar and above are amorphous, while films deposited under 0.75

mbar were polycrystalline. The origin of this difference must be the enhanced energetic bombardment at the lower pressures. This additional energy enhances adatom movement through the surface, that enables the polycrystalline arrangement of the growing film. At high pressure, this activation due to fast particle bombardment is reduced, and the film grows amorphous.

When we analyze the GIXRD results together with the resistivity we find that there is a correlation on the resistivity decrease with the polycrystalline/amorphous transition, being 0.75 mbar the turning point. In conventional magnetron sputtering systems the deposition pressure is much lower than 0.5 mbar (typically 10^{-2} – 10^{-3} mbar), and thus ITO films are typically polycrystalline, and the free carrier concentration is determined by Sn content and its activation [69]. On the other hand, in our samples deposited at 1.0 mbar and above, the films are amorphous and therefore the carrier concentration is mainly due to the O vacancies [70].

In the TCO literature, many works focus only on the resistivity value [59,67,74,75,79], without measuring carrier concentration and mobility. In our amorphous material it is important to measure these parameters, because a low mobility (due to the amorphous structure) for samples with also a low resistivity would lead to a excessively high carrier concentration. This would compromise near-infrared transparency due to free-carrier absorption [68]. As a reference, low temperature polycrystalline ITO typically presents mobilities under 20 $cm^2V^{-1}s^{-1}$, while annealing-optimized polycrystalline ITO had mobilities around 30–50 $cm^2V^{-1}s^{-1}$ [68,80]. This mobility is lower than the In_2O_3 bulk value, due to the strong hybridization of Sn and In s-orbitals that define the conduction band [60,81]. On the other hand, optimized amorphous ITO mobility can be comparable to In_2O_3 [69,82].

We measured the mobility and carrier density in the whole deposition pressure range by the van der Pauw method together with the Hall effect determination. Fig. 6 shows these results for the samples deposited at an *rf* power of 40 W as a function of deposition pressure, before and after the 30 min hot-plate anneal.

The first result for the as-deposited samples was that the van der Pauw measurements produced sheet resistance values that were consistent with the values obtained with the aligned 4-probe method. Also, the trend is that the carrier concentration increases with deposition pressure, with the only exception of the 0.5 mbar sample. This is the only one that is clearly polycrystalline, so we can justify this deviation from the trend by the polycrystalline structure of this film. For pressures above 1.0 mbar the electron concentration is quite high, in the

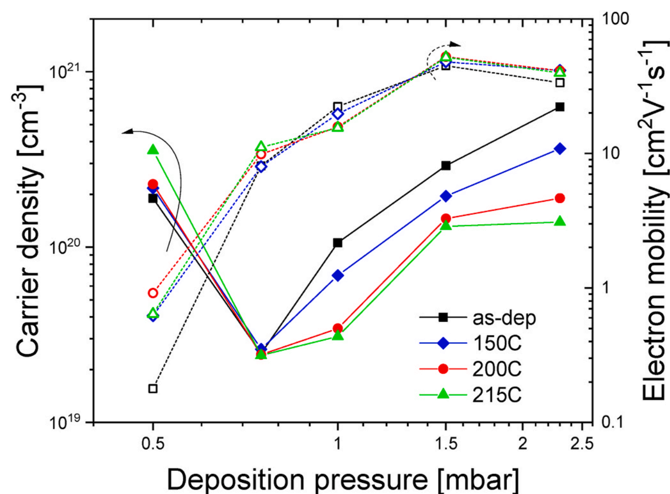

Fig. 6. Carrier density (filled symbols, left axis) and electron mobility (open symbols, right axis) of the ITO films as-deposited on glass substrates (squares), and after a 30 min anneal in air at 150 °C (diamonds), 200 °C (circles) and 215 °C (triangles) *color online.*

10^{20}–10^{21} cm^{-3} range. The maximum value is 6.3×10^{20} cm^{-3} for the 2.3 mbar sample, which is a very high value considering the amorphous character of the films. It is known that in polycrystalline ITO Sn doping is the main origin of free carrier density, while in amorphous ITO Sn does not play a major role, and it is the oxygen vacancy concentration the parameter that determines the electron density [70,71]. The trend of the carrier concentration shown in Fig. 6 agrees with this scenario: for low pressure we are detecting the Sn doping of polycrystalline ITO, while increasing the pressure produces films with more O_2 vacancies due to a reduced energy of the incoming species.

Focusing on mobility, its value increases with pressure up to a maximum of 45 $cm^2V^{-1}s^{-1}$ at 1.5 mbar, and slightly decreases at 2.3 mbar. An unexpected result was that the polycrystalline film presented the minimum mobility of the set, with a very low value of only 0.2 $cm^2V^{-1}s^{-1}$. This means that for this sample the electrons are dispersed by the grain boundaries, and this is the limiting factor for the mobility. On the other hand, the amorphous films present very high mobilities, with values comparable to optimized polycrystalline ITO films. In these films the limiting factor must be the ionized impurities (oxygen vacancies).

Thus, our results show that, in principle, the amorphous structure of the films growth at pressures of 1.0 mbar and above does not hinder its use on photovoltaic devices. As explained before, when choosing the deposition conditions between two films with similar resistivity values, the one with the higher mobility would be preferred.

Combining these results with the Sn/In results from XPS confirms that for amorphous ITO films having an adequate Sn content does not guarantee a high carrier concentration: the samples deposited at 0.75 mbar have an electron density of only 2.5×10^{19} cm^{-3}, while with comparable Sn content the samples deposited at 1.5 mbar have 2.9×10^{20} cm^{-3} electrons. These results show that for the HPS deposited amorphous ITO, the deposition pressure determines the oxygen vacancies and, thus, the carrier concentration.

To study the thermal stability of the films, we performed several consecutive hot-plate anneals in air at temperatures between 100 °C and 215 °C. After each anneal the van der Pauw and Hall effect measurements were repeated. Annealing at 100 °C in air with a hot plate for 30 min did not produce any relevant effect on the mobility and carrier concentration (not shown), indicating that the HPS ITO films were stable at typical cell operating conditions. On the other hand, annealing at higher temperatures affected mainly carrier concentration, with a small impact on mobility. The samples showed different trends depending on the crystal structure. The polycrystalline sample was the only sample that improved both mobility and carrier density and, thus, resistivity. However, for the samples with lowest resistivity values before annealing (1.5 and 2.3 mbar), the carrier concentration strongly decreases while the mobility slightly improves. This is consistent with the fact that oxygen vacancies are in the origin of the carrier concentration: annealing in air produces the oxidation of the amorphous films, reducing the amount of oxygen vacancies and therefore reducing carrier concentration.

The overall effect of these trends with temperature is that the resistivity increases since the mobility improvement does not fully compensate the carrier density loss. This trend is most severe for the 2.3 mbar sample, where the electron concentration decreases almost an order of magnitude. After annealing at 215 °C the best sample was the one deposited at 1.5 mbar, with a resistivity of 9×10^{-4} Ω cm. From a processing point of view, these results indicate that the incorporation of HPS deposited amorphous ITO on finished cells would require to keep the processing temperature in air as low as possible, to achieve the minimum resistivity.

For the successful integration of HPS ITO on a photovoltaic cell the films need to have good transparency on the visible and near-infrared region of the spectrum. To characterize the transparency, films with thicknesses ~100 nm were deposited on quartz substrates. Again, we focused on the samples where the change in resistivity was more

pronounced (0.75 mbar–1.5 mbar). The transmittance, specular reflectance, and absorptance of these samples in the visible and near infrared region are shown in Fig. 7.

From the fitting of these spectra the calculated thickness of the films was 88.1 nm (0.75 mbar), 134.2 nm (1.0 mbar) and 86.7 nm (1.5 mbar). Thus, the thicknesses of the films are in the typical range for photovoltaic cells.

We can observe that from the transparency standpoint there are no relevant differences between these samples: the films present a high transmittance value in the 70%–90% range in the visible region, with the typical oscillations due to interference. Focusing on the absorptance, it is negligible in the visible region (the small negative values are due to the measuring tool, that needs to be modified between T and R measurements, and thus the measuring region is not exactly the same for T and R). In the infrared region there is a small increase of the absorptance with pressure, which can be related to the increase of free carriers measured electrically. In any case, the absorptance is lower than 10% in the whole high wavelength region. The differences in resistivity do not have a relevant impact on the transmittance. We calculated the average transmission in the 350–1100 nm range weighted by the AM1.5G spectrum:

$$T_w = \frac{\int_{350}^{1100} T(\lambda) G_{AM1.5G}(\lambda) d\lambda}{\int_{350}^{1100} G_{AM1.5G}(\lambda) d\lambda} \quad (2)$$

The results of these calculations were very similar for the three films: 79.5% (0.75 mbar), 82.1% (1.0 mbar) and 79.1% (1.5 mbar). The growth rates that we obtained by optical measurements were consistent with the growth rates that we had previously determined with profilometry. The results of n and α were very similar for all three samples. As a reference, the refractive index at 1 eV was 1.91 (0.75 mbar), 1.90 (1.0 mbar) and 1.87 (1.5 mbar), while α was 4.8–5.5×10^4 cm^{-1} at 3.5 eV. From the α values we obtained the optical bandgaps by fitting to a Tauc law [61]. These fits are shown in Fig. 8.

The intercept with the abscissa axis gives the gap energy. In our samples, as expected from the transmittance results, the bandgap is very similar in all three films: 3.60 eV (0.75 mbar), 3.61 eV (1.0 mbar), and 3.83 eV (1.5 mbar). These values are within the variability of the Tauc representation and are in accordance with the results obtained in other works [59,83]. No clear Burstein-Moss displacement can be observed [84]. Thus, we can conclude that, although the ITO films deposited in this pressure range present quite different resistivities, there are no

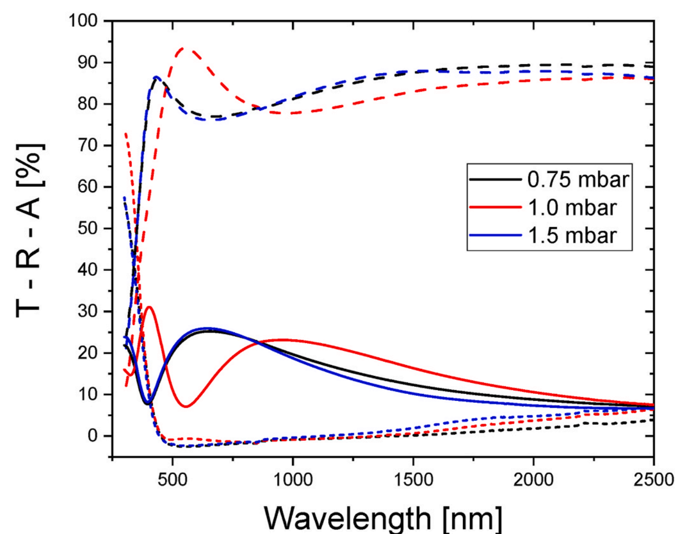

Fig. 7. Transmittance (dashed line), specular reflectance (solid line) and absorptance (dotted line) of ITO samples deposited at 40W of *rf* power and Ar pressure in the [0.75 mbar–1.5 mbar] range.

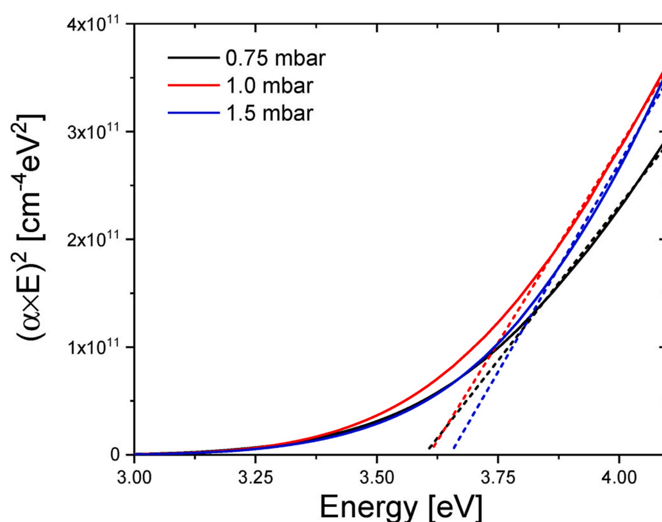

Fig. 8. Tauc plot of the absorption coefficient (solid lines) and linear fit, used to obtain the bandgap energy.

relevant differences in optical behavior. Also, all these films have a good transparency that makes them adequate for solar cell applications.

In Table II we summarize the most relevant results that we obtained for these films up to this point.

The results shown so far were obtained using glass or quartz substrates. This characterization is relevant for a general purpose ITO, but aiming at the use of HPS ITO films with DASH cells it is also important to characterize the electrical characteristics of the films when they are deposited on a-Si:H passivated c-Si. It is known that hydrogen effusion from the a-Si:H film when the samples are annealed at low temperature can induce modifications on the film atomic arrangement, thus producing changes on the electrical behavior. Fig. 9 shows the carrier concentration and mobility of the ITO films deposited on a-Si:H/c-Si/a-Si:H substrates as a function of annealing temperature.

While the overall trend for this set of samples is similar to the samples deposited on glass, there are some differences. The as-deposited films present higher mobilities that decrease with the annealing at 100 °C for the amorphous films, while for the 0.75 mbar ITO the mobility increases monotonically with annealing temperature. Also, this sample presents a higher electron concentration. The origin of the differences of the as-deposited films as compared with the glass substrate results is unclear, but it can be related to the difference on substrate temperature during deposition due to the different heat conductivity of Si and glass. Although the substrate holder reached roughly the same temperature, we do not have a direct measurement of the substrate surface.

As with glass substrates, the carrier density decreases with annealing temperature for all three samples, but with these c-Si substrates the decrease is more pronounced than for the glass substrate samples. In fact, after the 215 °C anneal, the resistivity of the 1.5 mbar sample degraded to 3 × 10^{-3} Ω cm, which indicates that H effusion from the a-Si:H plays a significant role in the ITO carrier concentration. Thus, to ensure that this effect is limited, a pre-deposition annealing step would be needed to promote lightly-bonded H effusion from the a-Si:H. In the future we will perform this study aiming at the optimization of HPS ITO for its use on HIT cells.

To sum up the results obtained up to this moment, we found that the films deposited at a pressure lower than 0.75 mbar were polycrystalline, while at high pressure were amorphous. For these amorphous samples Sn content does not impact carrier concentration, which must be due to oxygen vacancies. Although before annealing the film deposited at 2.3 mbar presents lower resistivity than the sample deposited at 1.5 mbar, it is at the expense of reduced mobility, and the impact of annealing

Table 2
Summary of the properties of ITO films deposited by HPS at 40 W.

Deposition Pressure (mbar)	Electron density (cm^{-3})	Mobility (cm^2/V.s)	Resistivity (Ω cm)	R. after 215 °C (Ω cm)	Growth rate (nm/min)	Refractive index @ 1 eV	Gap energy (eV)	$T_{AM1.5G}$
0.75	2.5×10^{19}	8.1	3.1×10^{-2}	2.3×10^{-2}	1.71	1.91	3.60	79.5%
1.0	1.1×10^{20}	22	2.6×10^{-3}	1.2×10^{-2}	1.45	1.90	3.61	82.1%
1.5	2.9×10^{20}	45	4.7×10^{-4}	9.1×10^{-4}	0.96	1.87	3.83	79.1%

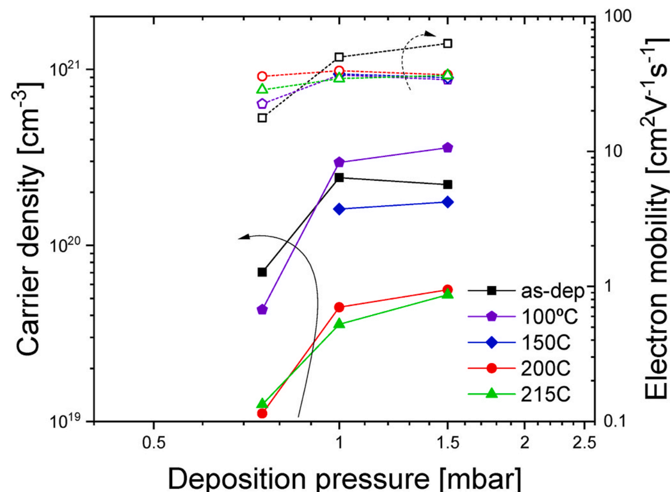

Fig. 9. Carrier density (filled symbols, left axis) and electron mobility (open symbols, right axis) of the ITO films as-deposited on a-Si:H/c-Si/a-Si:H passivated substrates (squares), and after a 30 min anneal in air at 100 °C (pentagons), 150 °C (diamonds), 200 °C (circles) and 215 °C (triangles) *color online*.

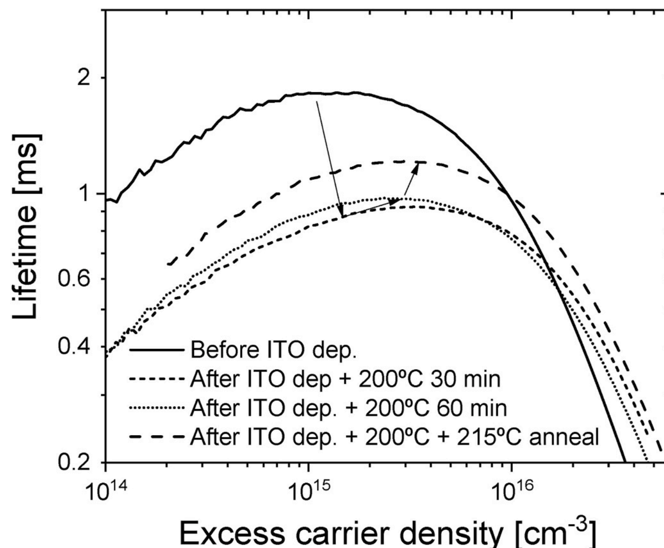

Fig. 10. Carrier lifetime measurements as a function of photogenerated excess carrier density of an a-Si:H passivated c-Si substrate before ITO deposition (solid line), after ITO deposition and annealing in air at 200 °C during 30 min (short dashed line), 60 min (dotted line) and after additional annealing at 215 °C for 30 min (long dashed line). The arrows are included to highlight the evolution with thermal budget.

temperature on resistivity was less severe for the film deposited at 1.5 mbar. The films deposited on a-Si:H/cSi/a-Si:H showed similar trends, but for annealing temperatures of 200 °C and above the resistivity was worse than the equivalent samples deposited on glass. Also, from a practical standpoint, at 2.3 mbar the plasma was unstable, and the growth rate was lower. This reduced growth rate implies that if we worked at 2.3 mbar, to deposit 75–80 nm the process would be longer, with the result of an increased UV irradiation to the sample. This UV irradiation can also impact cell performance. Thus, in the final part of the article we will focus on the amorphous ITO films deposited at 1.5 mbar.

As final test to check if the HPS deposited ITO films were suitable to be used in HIT solar cells, we deposited a ~80 nm thick ITO film on the top surface of a high quality c-Si sample passivated with undoped a-Si:H on both sides. The conditions chosen were the ones that showed the minimal resistivity after annealing for the glass and c-Si substrates: 1.5 mbar of Ar and 40 W of *rf* power. Fig. 10 shows the carrier lifetime measurements of the passivated sample before deposition. A maximum of 1.8 ms at an excess carrier density of 10^{15} cm^{-3} is observed. The 1 Sun iV_{oc} was 731 mV.

After ITO deposition the lifetime decreased several orders of magnitude, to a low value of 14 µs at an excess carrier density of 10^{15} cm^{-3}. This is due to the well-known a-Si:H degradation when it is exposed to UV radiation [85]. This damage is not permanent and can be recovered by low temperature annealing in air. The origin of the degradation is the Si–H bond breakage by UV radiation of the plasma that takes place without atomic displacement. Low temperature annealing can heal most of these broken bonds, as Fig. 10 shows. We performed several hot plate anneals at 200 °C. After 30 min annealing, the maximum lifetime increased drastically to 0.93 ms. After increasing the total annealing time to 1 h the lifetime only increased marginally, to 0.97 ms, with a 1 Sun iV_{oc} of 710 mV. This temperature and lifetime values are adequate for HIT cell fabrication, but in order to check if even higher temperatures produced an improved lifetime, we further annealed the sample for 30 min at 215 °C. We found that the lifetime increased to 1.2 ms, and the 1 Sun iV_{oc} was essentially recovered, with a value of 719 mV, that remained stable after several days.

To study the antireflective properties of the optimized HPS ITO film after the anneals, the hemispherical reflectance of the same sample as Fig. 10 was measured in the 300–2500 nm wavelength range, and the results are shown in Fig. 11.

We observe the typical characteristics of an antireflective coating on polished Si, with a reflectance minimum of only 0.8% at a wavelength of 656 nm. From the minimum of the reflectance we can calculate the thickness of the film using eq. (1), which produces a value of 79 nm. The weighted reflectance in the 350–1100 wavelength range was calculated by the expression:

$$R_{hem,w} = \frac{\int_{350}^{1100} R_{hem}(\lambda) G_{AM1.5G}(\lambda) d\lambda}{\int_{350}^{1100} G_{AM1.5G}(\lambda) d\lambda} \quad (3)$$

As a reference, while a polished Si wafer has a weighted reflectance around 45%, in our case the weighed value was 16.4%. This is a satisfactory value for untextured Si solar cells, thanks to the optimized ITO thickness.

Finally, through cross-sectional SEM we can observe the surface morphology to detect roughness, adhesion problems or evidence of crystallization. Fig. 12 shows the cross-sectional SEM image of the ITO film deposited on passivated Si after the annealing processes.

There is a clear contrast between the ITO film and the Si substrate. However, the a-Si:H film that is present between these layers is not distinguishable (its thickness is in the ~5 nm range). The film surface is

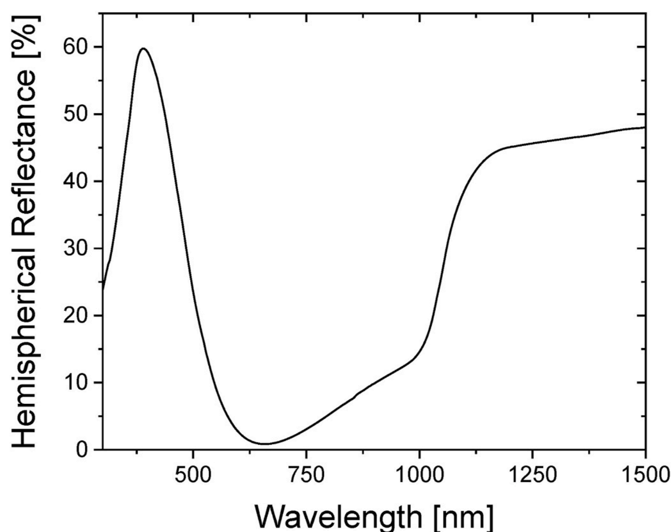

Fig. 11. Hemispherical reflectance of the a-Si:H passivated c-Si substrate after ITO deposition and annealing at 215 °C.

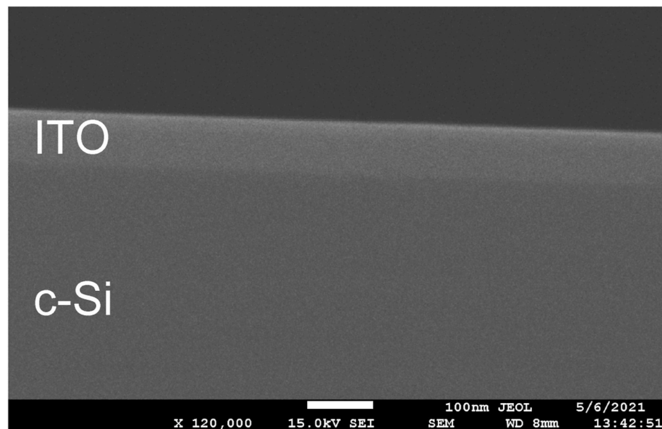

Fig. 12. Cross sectional SEM image of the ITO film deposited on a-Si:H passivated c-Si at 1.5 mbar with 40W of *rf* power.

flat and free of pinholes or irregularities. As expected from GIXRD results, there is no evidence of polycrystallinity in the image, such as columnar growth or surface topology. The surface is free of defects or bumps that would appear if there were adhesion problems [86]. The ITO thickness is 80 ± 3 nm, which is coherent with the optically measured thickness.

These results show that HPS deposited ITO has adequate properties to be used on the research of HIT solar cells in general and, in particular, in new structures with emerging selective contacts, such as the DASH cell.

4. Summary and conclusions

In this article we have shown the feasibility of the fabrication of ITO thin films by HPS of an ITO target in pure Ar atmosphere. The deposition pressure impacts strongly on the ITO resistivity value. At pressures above 1.0 mbar the as-deposited ITO films were amorphous and presented an adequate resistivity, lower than 10^{-3} Ω cm. The lowest value obtained was 3×10^{-4} Ωcm for 1.5 mbar. The mobility was quite high for an amorphous film, as expected from ITO, with a maximum value of 45 $cm^2V^{-1}s^{-1}$. The carrier concentrations were strongly dependent on deposition pressure and annealing temperature. In the 0.75–1.5 mbar range we did not measure any significant differences on Sn/In ratio (0.068–0.082), on the weighted transmittance (79.1–82.1%) or in the bandgap value (3.6–3.8 eV). As expected for amorphous ITO the most probable origin of the high carrier concentration are the oxygen vacancies, that are determined by growth dynamics and annealing. We also analyzed the impact of ITO deposition on a-Si:H passivated Si substrates by measuring mobility and carrier concentration, and we found that H effusion produced a severe decrease on carrier concentration for hot-plate annealing of 200 °C and above. Finally, we focused on the pressure that yielded more promising results, 1.5 mbar, and deposited a thickness-optimized film on a a-Si:H/c-Si/a-Si:H passivated substrate. After a low temperature annealing at 215 °C the 1Sun-iV_{oc} was 719 mV, and the weighted reflectance was 16.5%. SEM images of this sample confirmed the amorphous and uniform structure of the ITO film. All these results prove the feasibility of the use of HPS deposited ITO for the research of HIT cells.

Given that we found that low temperature air annealing affects HPS ITO properties, in the near future we will study the deposition at moderate substrate temperatures (under 250 °C), and the effect of hydrogen effusion from a-Si:H on carrier concentration and mobility. In any case, in this work we have shown that HPS is a promising technique for a single-tool deposition of the multilayer selective contact (selective layer + transport layer) needed for the research of non-conventional DASH cells.

Author statement

D. Caudevilla: Investigation, data curation, writing-review & editing, E. García-Hemme: Conceptualization, investigation, supervision, methodology, writing-review & editing. E. San Andrés: Conceptualization, data curation, funding acquisition, project administration, methodology, investigation, supervision, methodology, writing-original draft. F. Pérez-Zenteno: Investigation, data curation, writing-review. I. Torres: Investigation, data curation, formal analysis, writing-original draft. R. Barrio: Investigation, data curation, formal analysis, writing-original draft. R. García-Hernansanz: Investigation, writing-review & editing. S. Algaidy: Investigation, writing-review & editing. J. Olea: Investigation, writing-review & editing. D. Pastor: Investigation, writing-review. A. del Prado: funding acquisition, project administration, writing-review.

Declaration of competing interest

The authors declare that they have no known competing financial interests or personal relationships that could have appeared to influence the work reported in this paper.

Acknowledgements

The authors acknowledge the “CAI de Técnicas Físicas”, the “CAI de Difracción de Rayos X″ of Universidad Complutense de Madrid, and “Laboratorio de Caracterización de Superficies” of CENIM for sample fabrication, GIXRD and XPS measurements, respectively. Also we acknowledge J. Gandía for his support in the analysis of the optical measurements. This work is part of the project MADRID-PV2 (P2018/EMT-4308) funded by the Comunidad Autónoma de Madrid with the support from FEDER Funds, project TEC2017-84378-R, funded by MICINN and European Social Fund, and projects SCCell (PID2020-116508RB-I00), HyperPHIR (PID2020-117498RB-I00) and SCALED (PID2019-109215RB-C42), funded by the Spanish Ministry of Science and Innovation. D.Pastor acknowledges financial support from the MEC to the program Ramón y Cajal (No. RYC-2014-16936). D. Caudevilla would also acknowledge grant PRE2018-083798, financed by MICINN and European Social Fund.

References

[1] T. Mishima, M. Taguchi, H. Sakata, E. Maruyama, Development status of high-efficiency HIT solar cells. Solar Energy Materials and Solar Cells, North-Holland, 2011, pp. 18–21, https://doi.org/10.1016/j.solmat.2010.04.030.

[2] K. Masuko, M. Shigematsu, T. Hashiguchi, D. Fujishima, M. Kai, N. Yoshimura, T. Yamaguchi, Y. Ichihashi, T. Mishima, N. Matsubara, T. Yamanishi, T. Takahama, M. Taguchi, E. Maruyama, S. Okamoto, Achievement of more than 25% conversion efficiency with crystalline silicon heterojunction solar cell, IEEE Journal of Photovoltaics 4 (2014) 1433–1435, https://doi.org/10.1109/JPHOTOV.2014.2352151.

[3] M. Taguchi, Review—development history of high efficiency silicon heterojunction solar cell: from discovery to practical use, ECS Journal of Solid State Science and Technology 10 (2021) 25002, https://doi.org/10.1149/2162-8777/abdfb6.

[4] M. Taguchi, Y. Tsunomura, H. Inoue, S. Taira, T. Nakashima, T. Baba, H. Sakata, E. Maruyama, High-efficiency HIT solar cell on thin (<100um) silicon wafer, in: Proceedings of the 24th European Photovoltaic Solar Energy Conference, 2009, pp. 1690–1693.

[5] Y. Abdulraheem, I. Gordon, T. Bearda, H. Meddeb, J. Poortmans, Optical bandgap of ultra-thin amorphous silicon films deposited on crystalline silicon by PECVD, AIP Adv. 4 (2014) 57122, https://doi.org/10.1063/1.4879807.

[6] W.W. Jasruddin, T. Wenas, M. Winata, Barmawi, Growth study of wide bandgap a-Si:H and a-SiN:H by PECVD method for application in thin film transistor, in: IEEE International Conference on Semiconductor Electronics, Proceedings, ICSE, 2000, pp. 245–248, https://doi.org/10.1109/smelec.2000.932472.

[7] J. Bullock, Y. Wan, M. Hettick, X. Zhaoran, S.P. Phang, D. Yan, H. Wang, W. Ji, C. Samundsett, Z. Hameiri, D. Macdonald, A. Cuevas, A. Javey, Dopant-free partial rear contacts enabling 23% silicon solar cells, Advanced Energy Materials 9 (2019) 1803367, https://doi.org/10.1002/aenm.201803367.

[8] S. Patwardhan, B. Kavaipatti, Effect of ITO capping and its deposition parameters on electrical properties of MoO3/Si carrier-selective contact solar cell, INAE Letters (2019), https://doi.org/10.1007/s41403-018-0053-0.

[9] G. Gregory, C. Feit, Z. Gao, P. Banerjee, T. Jurca, O. Kristopher, Improving the passivation of molybdenum oxide hole-selective contacts with 1 nm hydrogenated aluminum oxide films for silicon solar cells, Phys. Status Solidi (2020) 1–6, https://doi.org/10.1002/pssa.202000093.

[10] P.K. Parashar, V.K. Komarala, Sputter deposited sub-stochiometric MoOx thin film as hole-selective contact layer for silicon based heterojunction devices, Thin Solid Films 682 (2019) 76–81, https://doi.org/10.1016/j.tsf.2019.05.004.

[11] J. Shi, L. Shen, Y. Liu, J. Yu, J. Liu, L. Zhang, Y. Liu, J. Bian, Z. Liu, F. Meng, MoOx modified ITO/a-Si:H(p) contact for silicon heterojunction solar cell application, Mater. Res. Bull. (2018), https://doi.org/10.1016/j.materresbull.2017.09.005.

[12] L.G. Gerling, S. Mahato, C. Voz, R. Alcubilla, J. Puigdollers, Characterization of transition metal oxide/silicon heterojunctions for solar cell applications, Appl. Sci. 5 (2015) 695–705, https://doi.org/10.3390/app5040695.

[13] G. Masmitjà, L.G. Gerling, P. Ortega, J. Puigdollers, I. Martín, C. Voz, R. Alcubilla, V2O: X-based hole-selective contacts for c-Si interdigitated back-contacted solar cells, J. Mater. Chem. 5 (2017) 9182–9189, https://doi.org/10.1039/c7ta01959a.

[14] U. Wurfel, A. Cuevas, P. Wurfel, Charge carrier separation in solar cells, IEEE Journal of Photovoltaics 5 (2015) 461–469, https://doi.org/10.1109/JPHOTOV.2014.2363550.

[15] U.W.P. Würfel, Physics of Solar Cells: from Basic Principles to Advanced Concepts, third ed., Wiley-VCH, Weinheim, Germany, 2016.

[16] K.A. Nagamatsu, S. Avasthi, G. Sahasrabudhe, G. Man, J. Jhaveri, A.H. Berg, J. Schwartz, A. Kahn, S. Wagner, J.C. Sturm, Titanium dioxide/silicon hole-blocking selective contact to enable double-heterojunction crystalline silicon-based solar cell, Appl. Phys. Lett. 106 (2015) 123906, https://doi.org/10.1063/1.4916540.

[17] R. Liu, S.T. Lee, B. Sun, 13.8% efficiency hybrid Si/organic heterojunction solar cells with MoO3 film as antireflection and inversion induced layer, Adv. Mater. 26 (2014) 6007–6012, https://doi.org/10.1002/adma.201402076.

[18] Y. Zhang, R. Liu, S.T. Lee, B. Sun, The role of a LiF layer on the performance of poly(3,4- ethylenedioxythiophene):poly(styrenesulfonate)/Si organic-inorganic hybrid solar cells, Appl. Phys. Lett. 104 (2014) 83514, https://doi.org/10.1063/1.4866968.

[19] J. Bullock, M. Hettick, J. Geissbühler, A.J. Ong, T. Allen, C.M. Sutter-Fella, T. Chen, H. Ota, E.W. Schaler, S. De Wolf, C. Ballif, A. Cuevas, A. Javey, Efficient silicon solar cells with dopant-free asymmetric heterocontacts, Nature Energy 1 (2016), https://doi.org/10.1038/nenergy.2015.31.

[20] J. Bullock, Y. Wan, Z. Xu, S. Essig, M. Hettick, H. Wang, W. Ji, M. Boccard, A. Cuevas, C. Ballif, A. Javey, Stable dopant-free asymmetric heterocontact silicon solar cells with efficiencies above 20%, ACS Energy Letters 3 (2018) 508–513, https://doi.org/10.1021/acsenergylett.7b01279.

[21] B. Lipovšek, F. Smole, M. Topič, I. Humar, A.R. Sinigoj, Driving forces and charge-carrier separation in p-n junction solar cells, AIP Adv. 9 (2019) 55026, https://doi.org/10.1063/1.5092948.

[22] A. Onno, C. Chen, P. Koswatta, M. Boccard, Z.C. Holman, Passivation, conductivity, and selectivity in solar cell contacts: concepts and simulations based on a unified partial-resistances framework, J. Appl. Phys. 126 (2019) 183103, https://doi.org/10.1063/1.5117201.

[23] R.A. Vijayan, S. Essig, S. De Wolf, B.G. Ramanathan, P. Loper, C. Ballif, M. Varadharajaperumal, Hole-collection mechanism in passivating metal-oxide contacts on Si solar cells: insights from numerical simulations, IEEE Journal of Photovoltaics 8 (2018) 473–482, https://doi.org/10.1109/JPHOTOV.2018.2796131.

[24] H. Mehmood, H. Nasser, T. Tauqeer, R. Turan, Simulation of silicon heterostructure solar cell featuring dopant-free carrier-selective molybdenum oxide and titanium oxide contacts, Renew. Energy 143 (2019) 359–367, https://doi.org/10.1016/j.renene.2019.05.007.

[25] H. Park, Y. Lee, S.J. Park, S. Bae, S. Kim, D. Oh, J. Park, Y. Kim, H. Guim, Y. Kang, H. Lee, D. Kim, J. Yi, Tunnel oxide passivating electron contacts for high-efficiency n-type silicon solar cells with amorphous silicon passivating hole contacts, Prog. Photovoltaics Res. Appl. 27 (2019) 1104–1114, https://doi.org/10.1002/pip.3190.

[26] A. Cuevas, Y. Wan, D. Yan, C. Samundsett, T. Allen, X. Zhang, J. Cui, J. Bullock, Carrier population control and surface passivation in solar cells, Sol. Energy Mater. Sol. Cell. 184 (2018) 38–47, https://doi.org/10.1016/j.solmat.2018.04.026.

[27] H. Hosono, D.C. Paine, D.S. Ginley, Handbook of Transparent Conductors, Media, Springer Science+Business, New York, 2011, https://doi.org/10.1007/978-1-4419-1638-9.

[28] J. Bullock, A. Cuevas, T. Allen, C. Battaglia, Molybdenum oxide MoOx: a versatile hole contact for silicon solar cells, Appl. Phys. Lett. 105 (2014), https://doi.org/10.1063/1.4903467.

[29] L. Ciacci, T.T. Werner, I. Vassura, F. Passarini, Backlighting the European indium recycling potentials, J. Ind. Ecol. 23 (2019) 426–437, https://doi.org/10.1111/jiec.12744.

[30] S.J.O. White, J.P. Shine, Exposure potential and health impacts of indium and gallium, metals critical to emerging electronics and energy technologies, Current Environmental Health Reports 3 (2016) 459–467, https://doi.org/10.1007/s40572-016-0118-8.

[31] J. Hu, R.G. Gordon, Textured aluminum-doped zinc oxide thin films from atmospheric pressure chemical-vapor deposition, J. Appl. Phys. 71 (1992) 880–890, https://doi.org/10.1063/1.351309.

[32] T. Minami, K. Oohashi, S. Takata, T. Mouri, N. Ogawa, Preparations of ZnO:Al transparent conducting films by d.c. magnetron sputtering, Thin Solid Films 193–194 (1990) 721–729, https://doi.org/10.1016/0040-6090(90)90224-2.

[33] Y. Geng, L. Guo, S.S. Xu, Q.Q. Sun, S.J. Ding, H.L. Lu, D.W. Zhang, Influence of Al doping on the properties of ZnO thin films grown by atomic layer deposition, J. Phys. Chem. C 115 (2011) 12317–12321, https://doi.org/10.1021/jp2023567.

[34] Z. Szabó, J. Volk, Z.E. Horváth, Z. Medveczky, Z. Czigány, K. Vad, Z. Baji, Atomic layer deposition and annealing of Ga doped ZnO films, Mater. Sci. Semicond. Process. 101 (2019) 95–102, https://doi.org/10.1016/j.mssp.2019.05.028.

[35] P.R. Chalker, P.A. Marshall, S. Romani, J.W. Roberts, S.J.C. Irvine, D.A. Lamb, A. J. Clayton, P.A. Williams, Atomic layer deposition of Ga-doped ZnO transparent conducting oxide substrates for CdTe-based photovoltaics, J. Vac. Sci. Technol.: Vacuum, Surfaces, and Films 31 (2013), https://doi.org/10.1116/1.4765642, 01A120.

[36] S.D. Ponja, S. Sathasivam, I.P. Parkin, C.J. Carmalt, Highly conductive and transparent gallium doped zinc oxide thin films via chemical vapor deposition, Sci. Rep. 10 (2020) 1–7, https://doi.org/10.1038/s41598-020-57532-7.

[37] P.C. Feijoo, M.A. Pampillón, E. San Andrés, J.L.G. Fierro, Nano-laminate vs. direct deposition of high permittivity gadolinium scandate on silicon by high pressure sputtering, Thin Solid Films 593 (2015) 62–66, https://doi.org/10.1016/j.tsf.2015.07.045.

[38] W. Xiaona, Z. Xinqiang, Y. Xiong, D.U. Jun, Y. Mengmeng, W. Lei, Fabrication and properties of Gd 2 O 3-doped HfO 2 high k film by Co-sputtering, Rare Met. 30 (2011) 647, https://doi.org/10.1007/s12598-011-0364-z.

[39] S. Wolf, Microchip Manufacturing, Lattice Press, Sunset Beack, CA, 2004.

[40] H.K. Kim, D.G. Kim, K.S. Lee, M.S. Huh, S.H. Jeong, K.I. Kim, T.Y. Seong, Plasma damage-free sputtering of indium tin oxide cathode layers for top-emitting organic light-emitting diodes, Appl. Phys. Lett. 86 (2005) 1–3, https://doi.org/10.1063/1.1923182.

[41] B. Demaurex, S. de Wolf, A. Descoeudres, Z. Charles Holman, C. Ballif, Damage at hydrogenated amorphous/crystalline silicon interfaces by indium tin oxide overlayer sputtering, Appl. Phys. Lett. 101 (2012), https://doi.org/10.1063/1.4764529.

[42] B.M. Meiners, D. Borchert, S. Hohage, S. Holinksi, P. Schäfer, Degradation of hydrogenated amorphous silicon passivation films caused by sputtering deposition, Physica Status Solidi (A) Applications and Materials Science 212 (2015) 1817–1822, https://doi.org/10.1002/pssa.201431923.

[43] V. Linss, M. Bivour, H. Iwata, K. Ortner, Comparison of low damage sputter deposition techniques to enable the application of very thin a-Si passivation films, in: AIP Conference Proceedings, American Institute of Physics Inc., 2019, p. 40009, https://doi.org/10.1063/1.5123836.

[44] M. Bivour, F. Zähringer, P. Ndione, M. Hermle, Sputter-deposited WOx and MoOx for hole selective contacts, in: Energy Procedia, Elsevier Ltd, 2017, pp. 400–405, https://doi.org/10.1016/j.egypro.2017.09.259.

[45] W. Umrath, Fundamentals of Vacuum Technology, Leybold, 1998.

[46] U. Poppe, J. Schubert, R.R. Arons, W. Evers, C.H. Freiburg, W. Reichert, K. Schmidt, W. Sybertz, K. Urban, Direct production of crystalline superconducting thin films of YBa2Cu3O7 by high-pressure oxygen sputtering, Solid State Commun. 66 (1988) 661–665, https://doi.org/10.1016/0038-1098(88)90228-1.

[47] E. San Andrés, M. Toledano-Luque, A. Del Prado, M.A. Navacerrada, I. Mártil, G. González-Díaz, W. Bohne, J. Röhrich, E. Strub, Physical properties of high pressure reactively sputtered TiO_2, J. Vac. Sci. Technol.: Vacuum, Surfaces and Films 23 (2005), https://doi.org/10.1116/1.2056554.

[48] M. Toledano-Luque, E. San Andrés, J. Olea, A. del Prado, I. Mártil, W. Bohne, J. Röhrich, E. Strub, Hafnium oxide thin films deposited by high pressure reactive sputtering in atmosphere formed with different Ar/O_2 ratios, Mater. Sci. Semicond. Process. 9 (2006), https://doi.org/10.1016/j.mssp.2006.10.018.

[49] Z. Gao, M.F. Romero, A. Redondo-Cubero, M.A. Pampillon, E. San Andres, F. Calle, Effects of Gd_2O_3 gate dielectric on proton-irradiated AlGaN/GaN HEMTs, IEEE Electron. Device Lett. 38 (2017), https://doi.org/10.1109/LED.2017.2682795.
[50] M.A. Pampillón, E. San Andrés, P.C. Feijoo, J.L.G. Fierro, High-k gadolinium scandate on Si obtained by high pressure sputtering from metal targets and in-situ plasma oxidation, Semicond. Sci. Technol. (2017) 32, https://doi.org/10.1088/1361-6641/aa58cc.
[51] J. Dréon, Q. Jeangros, J. Cattin, J. Haschke, L. Antognini, C. Ballif, M. Boccard, 23.5%-efficient silicon heterojunction silicon solar cell using molybdenum oxide as hole-selective contact, Nanomater. Energy 70 (2020) 104495, https://doi.org/10.1016/j.nanoen.2020.104495.
[52] J. Geissbühler, J. Werner, S. Martin De Nicolas, L. Barraud, A. Hessler-Wyser, M. Despeisse, S. Nicolay, A. Tomasi, B. Niesen, S. De Wolf, C. Ballif, 22.5% efficient silicon heterojunction solar cell with molybdenum oxide hole collector, Appl. Phys. Lett. 107 (2015) 81601, https://doi.org/10.1063/1.4928747.
[53] H. Mehmood, H. Nasser, T. Tauqeer, S. Hussain, E. Ozkol, R. Turan, Simulation of an efficient silicon heterostructure solar cell concept featuring molybdenum oxide carrier-selective contact, Int. J. Energy Res. 42 (2018) 1563–1579, https://doi.org/10.1002/er.3947.
[54] S. Bhatia, I.M. Khorakiwala, P.R. Nair, A. Antony, Influence of post deposition fabrication steps and quantitative estimation of band diagram of Si/MoOX heterojunction for carrier selective solar cells, Sol. Energy 194 (2019) 141–147, https://doi.org/10.1016/j.solener.2019.10.025.
[55] R. García-Hernansanz, E. García-Hemme, D. Montero, J. Olea, A. del Prado, I. Mártil, C. Voz, L.G. Gerling, J. Puigdollers, R. Alcubilla, Transport mechanisms in silicon heterojunction solar cells with molybdenum oxide as a hole transport layer, Sol. Energy Mater. Sol. Cell. 185 (2018) 61–65, https://doi.org/10.1016/j.solmat.2018.05.019.
[56] G. González-Díaz, D. Pastor, E. García-Hemme, D. Montero, R. García-Hernansanz, J. Olea, A. del Prado, E. San Andrés, I. Mártil, A robust method to determine the contact resistance using the van der Pauw set up, Measurement, Journal of the International Measurement Confederation 98 (2017) 151–158, https://doi.org/10.1016/j.measurement.2016.11.040.
[57] C.D. Wagner, L.E. Davis, M.V. Zeller, J.A. Taylor, R.H. Raymond, L.H. Gale, Empirical atomic sensitivity factors for quantitative analysis by electron spectroscopy for chemical analysis, Surf. Interface Anal. 3 (1981) 211–225, https://doi.org/10.1002/sia.740030506.
[58] J.L. Hernández-Rojas, M.L. Lucía, I. Mártil, G. González-Díaz, J. Santamaría, F. Sánchez-Quesada, Optical analysis of absorbing thin films: application to ternary chalcopyrite semiconductors, Appl. Opt. 31 (1992) 1606, https://doi.org/10.1364/ao.31.001606.
[59] M. Marikkannan, M. Subramanian, J. Mayandi, M. Tanemura, V. Vishnukanthan, J. M. Pearce, Effect of ambient combinations of argon, oxygen, and hydrogen on the properties of DC magnetron sputtered indium tin oxide films, AIP Adv. 5 (2015), https://doi.org/10.1063/1.4906566.
[60] S. Catalán, L. Álvarez-Fraga, E. Salas, R. Ramírez-Jiménez, A. Rodriguez-Palomo, A. De Andrés, C. Prieto, Charge mobility increase in indium-molybdenum oxide thin films by hydrogen doping, Appl. Surf. Sci. 386 (2016) 427–433, https://doi.org/10.1016/j.apsusc.2016.05.109.
[61] J. Tauc, R. Grigorovici, A. Vancu, Optical properties and electronic structure of amorphous germanium, Phys. Status Solidi 15 (1966) 627–637, https://doi.org/10.1002/pssb.19660150224.
[62] L. Zhao, Y.H. Zuo, C.L. Zhou, H.L. Li, H.W. Diao, W.J. Wang, Theoretical investigation on the absorption enhancement of the crystalline silicon solar cells by pyramid texture coated with SiNx:H layer, Sol. Energy 85 (2011) 530–537, https://doi.org/10.1016/j.solener.2010.12.020.
[63] O.S. Heavens, Optical Properties of Thin Solid Films, Butterworths Scientific Publications., 1955.
[64] R.A. Sinton, A. Cuevas, M. Stuckings, Quasi-steady-state photoconductance, a new method for solar cell material and device characterization. Conference Record of the IEEE Photovoltaic Specialists Conference, IEEE, 1996, pp. 457–460, https://doi.org/10.1109/pvsc.1996.564042.
[65] J.E. Sansonetti, W.C. Martin, Handbook of basic atomic spectroscopic data, J. Phys. Chem. Ref. Data 34 (2005) 1559–2259, https://doi.org/10.1063/1.1800011.
[66] A.G. Gaydon, The Identification of Molecular Spectra, Springer Netherlands, 1976.
[67] S.M.A. Durrani, E.E. Khawaja, J. Shirokoff, M.A. Daous, G.D. Khattak, M.A. Salim, M.S. Hussain, Study of Electron-Beam Evaporated Sn-Doped in 203 Films, 1996.
[68] G. Frank, H. Köstlin, Electrical properties and defect model of tin-doped indium oxide layers, Applied Physics A Solids and Surfaces 27 (1982) 197–206, https://doi.org/10.1007/BF00619080.
[69] Y. Shigesato, D.C. Paine, Study of the effect of Sn doping on the electronic transport properties of thin film indium oxide, Appl. Phys. Lett. 62 (1993) 1268–1270, https://doi.org/10.1063/1.108703.
[70] K. Okada, S. Kohiki, S. Luo, D. Sekiba, S. Ishii, M. Mitome, A. Kohno, T. Tajiri, F. Shoji, Correlation between resistivity and oxygen vacancy of hydrogen-doped indium tin oxide thin films, Thin Solid Films 519 (2011) 3557–3561, https://doi.org/10.1016/j.tsf.2011.01.249.
[71] H. Morikawa, M. Fujita, Crystallization and electrical property change on the annealing of amorphous indium-oxide and indium-tin-oxide thin films, Thin Solid Films 359 (2000) 61–67, https://doi.org/10.1016/S0040-6090(99)00749-X.
[72] J.R. Bellingham, W.A. Phillips, C.J. Adkins, Amorphous indium oxide, Thin Solid Films 195 (1991) 23–32, https://doi.org/10.1016/0040-6090(91)90255-V.
[73] J.R. Bellingham, W.A. Phillips, C.J. Adkins, Electrical and optical properties of amorphous indium oxide, J. Phys. Condens. Matter 2 (1990) 6207–6221, https://doi.org/10.1088/0953-8984/2/28/011.
[74] J. Gwamuri, M. Marikkannan, J. Mayandi, P.K. Bowen, J.M. Pearce, Influence of oxygen concentration on the performance of ultra-thin RF magnetron sputter deposited indium tin oxide films as a top electrode for photovoltaic devices, Materials 9 (2016), https://doi.org/10.3390/ma9010063.
[75] Z. Chen, W. Li, R. Li, Y. Zhang, G. Xu, H. Cheng, Fabrication of highly transparent and conductive indium-tin oxide thin films with a high figure of merit via solution processing, Langmuir 29 (2013) 13836–13842, https://doi.org/10.1021/la4033282.
[76] M.H. Ahn, E.S. Cho, S.J. Kwon, Effect of the duty ratio on the indium tin oxide (ITO) film deposited by in-line pulsed DC magnetron sputtering method for resistive touch panel, Appl. Surf. Sci. 258 (2011) 1242–1248, https://doi.org/10.1016/j.apsusc.2011.09.081.
[77] Y. Kobayashi, T. Shirochi, Y. Yasuda, T. Morita, Synthesis of silver/copper nanoparticles and their metal-metal bonding property, J. Min. Metall. B Metall. 49 (2013) 65–70, https://doi.org/10.2298/JMMB120927025K.
[78] J. Zemann, Crystal Structures, in: R.W.G. Wyckoff (Ed.), Acta Crystallographica, 2 nd edition vol. 1, 1965, pp. 7–83, https://doi.org/10.1107/s0365110x65000361, vol. 18.
[79] C. May, J. Strümpfel, ITO coating by reactive magnetron sputtering-comparison of properties from DC and MF processing, Thin Solid Films 351 (1999) 48–52, https://doi.org/10.1016/S0040-6090(99)00206-0.
[80] A. Valla, P. Carroy, F. Ozanne, D. Muñoz, Understanding the role of mobility of ITO films for silicon heterojunction solar cell applications, Sol. Energy Mater. Sol. Cell. 157 (2016) 874–880, https://doi.org/10.1016/j.solmat.2016.08.002.
[81] O.N. Mryasov, A.J. Freeman, Electronic band structure of indium tin oxide and criteria for transparent conducting behavior, Phys. Rev. B 64 (2001), https://doi.org/10.1103/PhysRevB.64.233111, 233111–1.
[82] M. Huang, Z. Hameiri, A.G. Aberle, T. Mueller, Study of hydrogen influence and conduction mechanism of amorphous indium tin oxide for heterojunction silicon wafer solar cells, Physica Status Solidi (A) Applications and Materials Science 212 (2015) 2226–2232, https://doi.org/10.1002/pssa.201532221.
[83] A. Tumbul, F. Aslan, A. Göktaş, I.H. Mutlu, All solution processed superstrate type Cu2ZnSnS4 (CZTS) thin film solar cell: effect of absorber layer thickness, J. Alloys Compd. 781 (2019) 280–288, https://doi.org/10.1016/j.jallcom.2018.12.012.
[84] I. Hamberg, C.G. Granqvist, K.-F. Berggren, B.E. Sernelius, L. Engström, Band-gap widening in heavily Sn-doped In2O3, Phys. Rev. B 30 (1984) 3240–3249, https://doi.org/10.1103/PhysRevB.30.3240.
[85] B. Demaurex, S. De Wolf, A. Descoeudres, Z. Charles Holman, C. Ballif, Damage at hydrogenated amorphous/crystalline silicon interfaces by indium tin oxide overlayer sputtering, Appl. Phys. Lett. 101 (2012), https://doi.org/10.1063/1.4764529.
[86] M.A. Pampillón, P.C. Feijoo, E. San Andrés, M.L. Lucía, A. del Prado, M. Toledano-Luque, Anomalous thermal oxidation of gadolinium thin films deposited on silicon by high pressure sputtering, Microelectron. Eng. 88 (2011), https://doi.org/10.1016/j.mee.2011.04.058.